Monthly Notices of the ROYAL ASTRONOMICAL SOCIETY

MNRAS **523,** 3119–3132 (2023) https://doi.org/10.1093/mnras/stad1470
Advance Access publication 2023 May 16

An empirical study of dust properties at the earliest epochs

Joris Witstok [1,2★] Gareth C. Jones,[3] Roberto Maiolino,[1,2,4] Renske Smit[5] and Raffaella Schneider [6,7,8]

[1]*Kavli Institute for Cosmology, University of Cambridge, Madingley Road, Cambridge CB3 0HA, UK*
[2]*Cavendish Laboratory, University of Cambridge, 19 JJ Thomson Avenue, Cambridge CB3 0HE, UK*
[3]*Department of Physics, University of Oxford, Denys Wilkinson Building, Keble Road, Oxford OX1 3RH, UK*
[4]*Department of Physics and Astronomy, University College London, Gower Street, London WC1E 6BT, UK*
[5]*Astrophysics Research Institute, Liverpool John Moores University, 146 Brownlow Hill, Liverpool L3 5RF, UK*
[6]*Dipartimento di Fisica, Sapienza, Università di Roma, Piazzale Aldo Moro 5, I-00185 Roma, Italy*
[7]*INFN, Sezione di Roma I, Piazzale Aldo Moro 2, I-00185 Roma, Italy*
[8]*INAF/Osservatorio Astronomico di Roma, Via di Frascati 33, I-00040 Monte Porzio Catone, Italy*

Accepted 2023 May 12. Received 2023 May 12; in original form 2022 November 21

ABSTRACT

We present an empirical analysis of the properties of dust-continuum emission in a sample of 17 galaxies in the early Universe ($4 < z < 8$) with well-sampled far-infrared spectral energy distributions (SEDs) compiled from the literature. We place our results into context by self-consistently comparing to samples of nearby star-forming galaxies, luminous infrared galaxies (LIRGs), and quasars. With the exception of two sources, we find no significant evolution in the dust emissivity index across cosmic time, measuring a consistent value of $\beta_{\rm IR} = 1.8 \pm 0.3$ at $z > 4$, suggesting that the effective dust properties do not change dramatically for most galaxies. Despite having comparable stellar masses, we find the high-redshift galaxies to be similar to, or even more extreme than, LIRGs in the *Herschel* (U)LIRG Survey, where (U)LIRG refers to (ultra-)LIRG, sample in terms of dust temperature ($T_{\rm dust} > 40$ K) and infrared (IR) luminosity ($L_{\rm IR} > 10^{11}$ L$_\odot$). We find that the dust temperature evolves mildly towards high redshift, though the LIRGs and quasars exhibit elevated temperatures indicating a more efficient and/or additional heating mechanism. Where available, we compare stellar mass estimates to our inferred dust masses, whose degeneracy with dust temperature can only be mitigated with a well-constrained SED. In merely half of the cases, the dust yield may be explained by supernovae alone, with four sources (44 per cent) significantly exceeding a highly optimistic yield where $M_{\rm dust} \approx 0.01 M_*$. We discuss possible explanations for this apparent inconsistency and potential observational biases in the measurements of the dust properties of high-redshift galaxies, including in the current IR-bright sample.

Key words: methods: observational – dust, extinction – galaxies: high-redshift – dark ages, reionization, first stars.

1 INTRODUCTION

Cosmic dust grains are a prominent agent in the physical processes governing galaxy formation and evolution on the scale of the interstellar medium (ISM). Dust catalyses the formation of molecules (Wakelam et al. 2017; Chen et al. 2018) and the fragmentation of gas clouds (Omukai et al. 2005; Schneider et al. 2006), two mechanisms that are essential to star formation. Furthermore, while the dust mass of a galaxy is negligible compared to its stellar or gas mass (Dwek 1998; Draine et al. 2007; Watson 2011), dust grains absorb a significant fraction of the optical and ultraviolet (UV) light and in the infrared (IR) thermally re-emit the absorbed energy (e.g. Savage & Mathis 1979; Draine 1989, 2003; Meurer, Heckman & Calzetti 1999; Calzetti et al. 2000; Weingartner & Draine 2001). This process has been shown to occur even among the first galaxies to emerge in the epoch of reionization (EoR; e.g. Laporte et al. 2017; Tamura et al. 2019; Bakx et al. 2020; Fudamoto et al. 2021).

A general consensus has been established on the various channels via which dust is formed across cosmic time. Specifically, the main sites of dust creation are thought to be asymptotic giant branch (AGB) stars, supernova (SN) events, and grain growth in the ISM (e.g. Mancini et al. 2015; Graziani et al. 2020; Dayal et al. 2022). However, it is still unclear what is the exact composition and abundance of dust, particularly in the early Universe, when the age of the Universe was comparable to typical dust formation time-scales (Todini & Ferrara 2001; Bianchi & Schneider 2007; Leśniewska & Michałowski 2019; Sommovigo et al. 2020; Witstok et al. 2023). In addition, we do not yet fully understand how grain growth occurs in the ISM. It has been shown that this requires very small grains, with sizes smaller than 10 nm, in the cold neutral medium (Draine 2009; Zhukovska et al. 2016), and that once the grains are incorporated in dense molecular clouds, their growth becomes problematic due to the formation of icy mantles (Ferrara, Viti & Ceccarelli 2016; Ceccarelli et al. 2018). As a result, there exists significant observational uncertainty on fundamental galaxy properties such as the star formation rate (SFR), especially when they are inferred exclusively from rest-frame UV and optical measurements (e.g. Madau & Dickinson 2014). Indeed, recent works suggest that a significant fraction of obscured star formation

★ E-mail: jnw30@cam.ac.uk

Table 1. Properties of local-Universe galaxy samples considered in this work.

Sample	Galaxy type	z	M_* ($M_\odot$)	$A_{\rm dust}$ (kpc^2)	$n_{\rm phot}$	References
JINGLE	SFG	$0.028^{+0.011}_{-0.006}$	$1.3^{+2.9}_{-1.0} \times 10^{10}$	$1.3^{+1.9}_{-0.8} \times 10^{2}$	5	Saintonge et al. (2018), Smith et al. (2019), Lamperti et al. (2019)
HERUS	(U)LIRG	$0.086^{+0.048}_{-0.043}$	$9.0^{+9.0}_{-5.0} \times 10^{10}$	$2.2^{+2.5}_{-1.9} \times 10^{3}$	5	Sanders et al. (2003), Clements et al. (2018)
PG	QSO	$0.14^{+0.19}_{-0.08}$	–	–	6	Petric et al. (2015)

Notes. Listed properties are their type (see Section 2.1), redshift (z), stellar mass (M_*) and area of the dust emission ($A_{\rm dust}$), number of photometric detections used for the fitting routine ($n_{\rm phot}$), and references to the relevant works describing the survey. Quantities quoted are median values with error bars reflecting the 16th and 84th percentiles.

activity may be missed (Fudamoto et al. 2020, 2021; Schaerer et al. 2020; Ferrara et al. 2022; Sommovigo et al. 2022b).

With the advent of the Atacama Large Millimeter/submillimeter Array (ALMA), the first statistical samples of galaxies in the EoR detected by their dust-continuum emission are starting to be assembled (e.g. Inami et al. 2022; Schouws et al. 2022). Nearly all of these sources, however, are only observed in a single photometric band, making it difficult to retrieve properties of the dust (Sommovigo et al. 2021, 2022a). Typically, the spectral energy distribution (SED) is modelled as a modified blackbody ('greybody'; see Witstok et al. 2022), assigning ensemble properties to the dust through the temperature and emissivity parameters, $T_{\rm dust}$ and $\beta_{\rm IR}$, which are commonly assumed for galaxies with few photometric detections in the far-IR (FIR).

In this work, instead, we compile a list of high-redshift sources with well-sampled FIR SEDs. We particularly focus on the dust emissivity power-law index $\beta_{\rm IR}$, which is connected to the microscopic properties of grains and therefore potentially holds the key to uncovering their evolutionary pathways (e.g. Jones et al. 2013). Furthermore, we investigate the dust mass and temperature, which become degenerate for poorly sampled SEDs, but have the potential of revealing the main origin of a galaxy's dust content built up over relatively short time-scales (e.g. Michałowski 2015; Graziani et al. 2020; Dayal et al. 2022). In Section 2, we briefly describe this sample and two other samples of galaxies in the local Universe. Section 3 describes the results of our analysis and discusses them in light of dust evolutionary mechanisms and potential changes in the properties of dust across cosmic time. Section 4 provides the conclusions of our findings. We adopt the cosmological parameters $\Omega_{\rm m} = 0.3$, $\Omega_\Lambda = 0.7$, and $H_0 = 70\,{\rm km\,s^{-1}\,Mpc^{-1}}$ throughout.

2 METHODS

We consider spectroscopically confirmed galaxies that are confidently detected in at least four rest-frame FIR photometric bands and have a (deconvolved) dust-continuum size measurement; for the purpose of fitting greybody curves to the dust emission, we consider a rest-frame FIR wavelength range of $10\ \mu{\rm m} \lesssim \lambda_{\rm emit} \lesssim 10^3\ \mu{\rm m}$. Nearby galaxies used for comparison are discussed in Section 2.1, while Section 2.2 describes the sources in the early Universe ($4 < z < 8$). We stress that caution has to be taken in interpreting the properties of our sample due to its diversity, as will be discussed in more detail.

2.1 Samples in the local Universe

The James Clerk Maxwell Telescope (JCMT) dust and gas In Nearby Galaxies Legacy Exploration (JINGLE) survey observed 192 nearby galaxies with *Herschel* (Saintonge et al. 2018; Lamperti et al. 2019; Smith et al. 2019). We make use of photometry at 100 and 160 μm (taken by *Herschel*/PACS) and at 250, 350, and 500 μm (*Herschel*/SPIRE), excluding the 22, 60, and 850 μm bands given potential mid-IR (MIR) excess due to hot dust surrounding active galactic nuclei (AGNs) and a non-thermal contribution to the low-frequency emission (some galaxies are not classified as purely star forming; however, for simplicity we apply this label since the sample does not contain bright AGNs; see Saintonge et al. 2018). Following Lamperti et al. (2019), we discard JINGLE-62 given its non-detection at 250 μm.

A second survey, the *Herschel* (U)LIRG Survey (HERUS), comprises 43 nearby (ultra-)luminous IR galaxies or (U)LIRGs observed by the *Infrared Astronomical Satellite* (*IRAS*) at 100 and 160 μm (Sanders et al. 2003), followed up by *Herschel*/SPIRE in the 250, 350, and 500 μm bands (Clements et al. 2018). We exclude 3C273 and IRAS 13451+1232 whose photometric measurements are not fit well by a greybody SED.

Thirdly, we consider a sample of nearby quasars (quasi-stellar objects or QSOs) selected from the Palomar–Green (PG) survey (Petric et al. 2015). We use the available FIR photometry at 70, 100, and 160 μm (taken by *Herschel*/PACS) and at 250, 350, and 500 μm (*Herschel*/SPIRE).

Due to the low spatial resolution of *Herschel*, the size of the dust-continuum emission ($A_{\rm dust}$, discussed further in Sections 2.2 and 2.3) in the samples of local objects is assumed to be equal to the optical size of the galaxy, if available. The properties of all three samples are summarized in Table 1.

2.2 High-redshift sample

We briefly summarize all 17 high-redshift galaxies and the literature works from which we acquired their compiled FIR SEDs in Table 2. The sources include six QSOs, eight star-forming galaxies (SFGs), and three submillimetre galaxies (SMGs). Size measurements of the dust-continuum emission ($A_{\rm dust}$), used to construct a self-consistent opacity model,[1] are taken by combining all reported deconvolved sizes. As will be discussed in Section 2.3, we note that these sizes are merely used to inform a first-order approximation of the optical depth as these necessarily correspond to slightly different wavelengths in the rest frame (which, as a result of non-uniform temperature distributions, indeed impacts the measured size; e.g. Akins et al. 2022; Witstok et al. 2022). We note that due to our requirement of having a dust-continuum size measurement, we do not include sources from the South Pole Telescope (SPT) survey (Reuter et al.

[1]Throughout this work, any discussion of opacity (and optically thin or thick cases) refers to the optical depths in the FIR unless specifically stated otherwise.

Table 2. Properties of high-redshift sources considered in this work.

Source	Type	z	M_* ($M_\odot$)	$A_{\rm dust}$ (kpc^2)	$n_{\rm phot}$	References
GN20	SMG	4.0553	$1.1^{+0.6}_{-0.4} \times 10^{11}$	50.3	6	(4), (8), (12)
GN20.2b	SMG	4.0563	$1.1^{+0.6}_{-0.4} \times 10^{11}$	31.4	4	(12)
ID141	SMG	4.243	···	4.8	10	(7), (26)
MORA-3	SFG	4.63	···	16.6	9	(5), (9), (22), (28), (34)
GN10	SFG	5.303	$1.2^{+0.1}_{-0.1} \times 10^{11}$	0.8	11	(31)
SPT0346−52	SFG	5.656	···	1.8	17	(15), (29)
MORA-4	SFG	5.85	$3.2^{+1.0}_{-1.5} \times 10^{9}$	1.8	10	(21), (34)
J2310+1855	QSO	6.0031	7.2×10^{9}	4.5	11	(18), (20), (24), (30), (38)
J1319+0959	QSO	6.133	···	8.8	7	(17), (20)
J0100+2802	QSO	6.327	···	11.3	9	(25), (39)
HFLS3	SFG	6.3369	3.7×10^{10}	4.9	28	(10)
J1148+5251	QSO	6.4189	···	7.1	8	(1), (2), (3), (6), (11), (13), (20)
SPT0311−58W	SFG	6.9	···	78.5	7	(19), (35)
SPT0311−58E	SFG	6.9	$3.5^{+1.5}_{-1.5} \times 10^{10}$	78.5	7	(19), (35)
A1689-zD1	SFG	7.13	$1.7^{+0.7}_{-0.5} \times 10^{9}$	1.9	4	(14), (16), (27), (33), (36)
GNz7q	QSO	7.1899	$2.5^{+1.4}_{-1.4} \times 10^{10}$	0.7	4	(37)
J1342+0928	QSO	7.54	···	9.4	7	(23), (32)

Notes. Listed properties are their type, redshift (z), estimates of the stellar mass (M_*) and measured deconvolved area of the dust emission ($A_{\rm dust}$), number of photometric detections used for the fitting routine ($n_{\rm phot}$), and references to the works from which we acquired the FIR photometry. References: (1) Bertoldi et al. (2003), (2) Robson et al. (2004), (3) Beelen et al. (2006), (4) Pope et al. (2006), (5) Younger et al. (2007), (6) Riechers et al. (2009), (7) Cox et al. (2011), (8) Magdis et al. (2011), (9) Casey et al. (2013), (10) Riechers et al. (2013), (11) Gallerani et al. (2014), (12) Tan et al. (2014), (13) Cicone et al. (2015), (14) Watson et al. (2015), (15) Aravena et al. (2016), (16) Knudsen et al. (2017), (17) Shao et al. (2017), (18) Feruglio et al. (2018), (19) Marrone et al. (2018), (20) Carniani et al. (2019), (21) Casey et al. (2019), (22) Magnelli et al. (2019), (23) Novak et al. (2019), (24) Shao et al. (2019), (25) Wang et al. (2019), (26) Cheng et al. (2020), (27) Inoue et al. (2020), (28) Jiménez-Andrade et al. (2020), (29) Jones et al. (2020), (30) Li et al. (2020), (31) Riechers et al. (2020), (32) Venemans et al. (2020), (33) Bakx et al. (2021), (34) Casey et al. (2021), (35) Jarugula et al. (2021), (36) Akins et al. (2022), (37) Fujimoto et al. (2022), (38) Tripodi et al. (2022), and (39) Tripodi et al. (2023).

2020) except SPT0346−52 and SPT0311−58, which have been observed separately (Aravena et al. 2016; Marrone et al. 2018; Jones et al. 2020; Jarugula et al. 2021). We do, however, consider the other SPT sources in our discussion of dust temperatures (Section 3.2). Similar to the JINGLE and HERUS photometries (Section 2.1), we excluded by visual inspection among the high-redshift sample those MIR and radio photometric measurements that clearly have a non-thermal origin and go beyond a simple modified-blackbody SED (see Appendix A, where we present the SEDs). Estimates of the stellar mass (M_*), if available, were derived from SED fitting in the works listed under a Chabrier (2003) initial mass function (IMF), except for J2310+1855 and GNz7q where they represent the dynamical mass minus the gas mass, $M_* \simeq M_{\rm dyn} - M_{\rm gas}$. The number of photometric detections, $n_{\rm phot}$, does not count upper limits (or data points that were excluded, as explained in Section 2.3).

2.3 Dust SED-fitting procedure

To derive the dust properties of each galaxy in the three samples discussed above, we fit a greybody SED with a self-consistent opacity model to the photometry with the Bayesian code MERCURIUS, presented in Witstok et al. (2022).[2] The derived dust properties of the high-redshift sample are shown in Table 3. We present all SEDs and an example of the obtained posterior distributions in Appendix A.[3]

Briefly, we performed two types of fits: either in an entirely optically thin scenario (dashed lines) or with a self-consistent general opacity model, where we link the dust mass surface density, derived using the measured deconvolved area corresponding to the dust emission ($A_{\rm dust}$; see Table 2), to the optical depth (see Witstok et al. 2022, for details). We note that for moderate- and low-resolution measurements where $A_{\rm dust}$ (even though it is deconvolved) may effectively represent an upper limit, the general opacity model only marginally differs from an optically thin SED due to the low dust surface mass density. A more accurate treatment of the optical depth would require modelling high-resolution images with detailed, three-dimensional radiative transfer models (e.g. Inoue et al. 2020; Hirashita & Chiang 2022), which is beyond the scope of this work. The estimated dust emissivity index is not significantly impacted by the choice of opacity model. The dust temperature, and hence the inferred dust mass, however, are more susceptible to changes in the opacity (see e.g. Cortzen et al. 2020; Riechers et al. 2020; Jin et al. 2022). In some cases, the general opacity model indeed produces notably better results than assuming that the SED is entirely optically thin (e.g. GN10 and SPT0346−52; see Appendix A). In the latter case, the a posteriori (AP) transition wavelength inferred is inconsistent with an optically thin scenario (see also Jones et al. 2020). For this reason, we opt for the self-consistent treatment as the fiducial model with the exception of the PG sample, where we fix the transition wavelength to $\lambda_0 = 200$ μm (having verified that an optically thin model only has a minor impact on our findings). Our measurement of the dust mass assumes a fixed dust absorption cross-section κ_ν appropriate for dust ejected by SNe after reverse-shock destruction (Hirashita et al. 2014), with the systematic uncertainty that could lower dust masses by ∼3× or increase them by ∼1.5×.

[2] Available at https://github.com/joriswitstok/mercurius/.

[3] Posterior distributions for the rest of our sample are presented as Supplementary material.

Table 3. Results from the MERCURIUS greybody fitting procedure of high-redshift sources discussed in Section 2.3.

Source	$M_{\rm dust}$ (10^7 M$_\odot$)	$T_{\rm dust}$ (K)	$T_{\rm peak}$ (K)	$\beta_{\rm IR}$	λ_0 (μm)	$L_{\rm IR}$ (10^{11} L$_\odot$)
GN20	358^{+53}_{-47}	37^{+1}_{-1}	34^{+1}_{-1}	$1.9^{+0.1}_{-0.1}$	55^{+4}_{-4}	152^{+13}_{-13}
GN20.2b	127^{+117}_{-40}	39^{+5}_{-10}	36^{+4}_{-9}	$1.8^{+0.2}_{-0.2}$	39^{+17}_{-7}	69^{+41}_{-45}
ID141	173^{+12}_{-11}	52^{+1}_{-1}	35^{+1}_{-1}	$1.91^{+0.07}_{-0.07}$	128^{+5}_{-4}	163^{+8}_{-8}
MORA-3	138^{+25}_{-20}	41^{+2}_{-2}	36^{+2}_{-2}	$1.8^{+0.1}_{-0.1}$	55^{+5}_{-5}	89^{+13}_{-12}
GN10	81^{+13}_{-11}	80^{+2}_{-2}	45^{+1}_{-1}	$2.7^{+0.2}_{-0.2}$	201^{+11}_{-10}	176^{+20}_{-20}
SPT0346−52	146^{+4}_{-3}	$80.3^{+0.4}_{-0.4}$	46^{+0}_{-1}	$1.65^{+0.02}_{-0.02}$	202^{+3}_{-3}	411^{+8}_{-8}
MORA-4	66^{+11}_{-10}	50^{+2}_{-2}	34^{+3}_{-2}	$1.88^{+0.10}_{-0.10}$	129^{+11}_{-11}	51^{+9}_{-6}
J2310+1855	136^{+3}_{-3}	$55.9^{+0.3}_{-0.3}$	$38.2^{+0.3}_{-0.4}$	$1.83^{+0.03}_{-0.03}$	116^{+2}_{-1}	196^{+4}_{-4}
J1319+0959	132^{+30}_{-28}	43^{+4}_{-3}	35^{+3}_{-2}	$1.7^{+0.2}_{-0.2}$	76^{+9}_{-10}	88^{+19}_{-14}
J0100+2802	25^{+4}_{-4}	46^{+3}_{-2}	45^{+2}_{-2}	$2.3^{+0.2}_{-0.2}$	40^{+3}_{-3}	59^{+9}_{-7}
HFLS3	230^{+8}_{-8}	64^{+1}_{-1}	39^{+1}_{-1}	$1.81^{+0.04}_{-0.04}$	147^{+3}_{-3}	414^{+17}_{-17}
J1148+5251	33^{+7}_{-6}	64^{+7}_{-6}	54^{+5}_{-5}	$1.7^{+0.2}_{-0.2}$	37^{+5}_{-4}	241^{+76}_{-60}
SPT0311−58W	179^{+46}_{-35}	46^{+4}_{-3}	40^{+2}_{-2}	$1.4^{+0.2}_{-0.1}$	18^{+3}_{-2}	227^{+28}_{-27}
SPT0311−58E	37^{+9}_{-7}	40^{+3}_{-3}	40^{+2}_{-2}	$2.0^{+0.2}_{-0.2}$	15^{+2}_{-1}	35^{+4}_{-4}
A1689-zD1	$1.9^{+1.0}_{-0.6}$	42^{+6}_{-5}	39^{+4}_{-4}	$1.8^{+0.2}_{-0.2}$	17^{+5}_{-3}	$1.9^{+0.5}_{-0.4}$
GNz7q	6^{+4}_{-2}	64^{+12}_{-11}	51^{+10}_{-10}	$1.8^{+0.2}_{-0.2}$	56^{+18}_{-11}	35^{+30}_{-18}
J1342+0928	4^{+4}_{-2}	56^{+23}_{-13}	55^{+20}_{-11}	$1.9^{+0.2}_{-0.2}$	12^{+5}_{-4}	26^{+52}_{-14}

Notes. Columns show the derived dust mass ($M_{\rm dust}$), dust temperature ($T_{\rm dust}$), peak temperature ($T_{\rm peak}$), dust emissivity index ($\beta_{\rm IR}$), opacity transition wavelength (λ_0), and total IR luminosity ($L_{\rm IR}$; between 8 and 1000 μm). Reported quantities are given as the median (i.e. 50th percentile) of the parameter's marginalized posterior distribution, with a $\pm1\sigma$ confidence range reflecting the 16th and 84th percentiles.

3 RESULTS AND DISCUSSION

3.1 Evolution and dependence of the dust emissivity index at $4 < z < 8$

First, we focus on the dust emissivity index, $\beta_{\rm IR}$. We show its redshift evolution in Fig. 1. GN10, with $\beta_{\rm IR} \simeq 2.7$, and to a similar extent J0100+2802 with $\beta_{\rm IR} \simeq 2.3$, appear to be clear anomalies compared to the rest of the galaxies analysed here. We note Riechers et al. (2020) and Tripodi et al. (2023) derive similarly extreme values for the dust emissivity index, which indicates that GN10 and J0100+2802 possess exceptional dust properties.

Otherwise, we measure mean dust emissivity index values consistent across the JINGLE, HERUS, and high-redshift samples ($\beta_{\rm IR} \simeq 1.8$) while slightly lower for the PG sample ($\beta_{\rm IR} \simeq 1.6$). We note that the high-redshift sample will likely have a selection bias towards the brightest IR sources, especially because of our requirement of having four confident detections. This may introduce a bias towards low values of $\beta_{\rm IR}$ (at fixed dust mass and temperature); however, this effect becomes weak at moderately high dust temperatures ($T_{\rm dust} \gtrsim 40$ K). To explore further such biases and potential differences between sources at low and high redshifts, Fig. 2 shows the interdependence of several dust properties: the dust emissivity index $\beta_{\rm IR}$, temperature ($T_{\rm dust}$), mass ($M_{\rm dust}$), and the total IR luminosity ($L_{\rm IR}$).

The top left panel illustrates a hint of anticorrelation between the dust emissivity index and temperature among the local samples (mainly in the HERUS sample, $p \approx 0.02$). This well-known degeneracy has been shown to artificially arise from least-squares fitting methods and can be circumvented by hierarchical Bayesian frameworks (e.g. Kelly et al. 2012; Lamperti et al. 2019). Indeed, MERCURIUS is designed to evaluate a likelihood based on the (weighted) sum of squared residuals (Witstok et al. 2022) so that such an artificial spread due to degeneracy may be expected; however, we note that it is unclear whether a hierarchical Bayesian approach is appropriate for our high-redshift sample, given its kaleidoscopic nature. Moreover, in this context we are mainly interested in any collective properties of our sample rather than precise individual measurements.

Interestingly, the high-redshift sample best aligns in all panels with the sample of local (U)LIRGs and QSOs, which are offset to higher dust temperatures relative to the JINGLE sample. At the same time, the high-redshift galaxies display more extreme dust masses and IR luminosities than both local galaxy samples. This is certainly (in part) the result of selection bias, since for galaxies in the distant Universe only the bright(er) sources can be discovered and detected across multiple wavelength bands within viable observing times. Still, it is worth noting that already in the first 2 Gyr of cosmic time these objects are able to form dust masses comparable to, or even larger than, the local galaxies considered here. In the next section, we will discuss the dust temperatures and masses in more detail.

3.2 Dust temperatures at $4 < z < 8$

The dust temperature has a large impact on derived IR luminosities and SFRs, but it can only be constrained with multiband FIR observations (e.g. Faisst et al. 2020; Bakx et al. 2021; Witstok et al. 2022; Algera et al. 2023). For this reason, both measurements and models of the dust temperature in the early Universe have been scrutinized in recent studies (e.g. Bouwens et al. 2020; Pallottini et al. 2022; Shen et al. 2022; Vijayan et al. 2022). A major hurdle in reconciling theory and observations is the fact that except for an optically thin SED with $\beta_{\rm IR} = 2$, the observed peak temperature $T_{\rm peak}$ is not trivially related to the dust temperature inferred from the SED, $T_{\rm dust}$ (let alone the luminosity- or mass-weighted dust temperature; e.g. Liang et al. 2019). In general, disentangling the effects of varying the dust temperature $T_{\rm dust}$ and opacity for an optically thick SED requires the SED to be probed at multiple wavelengths (Casey, Narayanan & Cooray 2014).

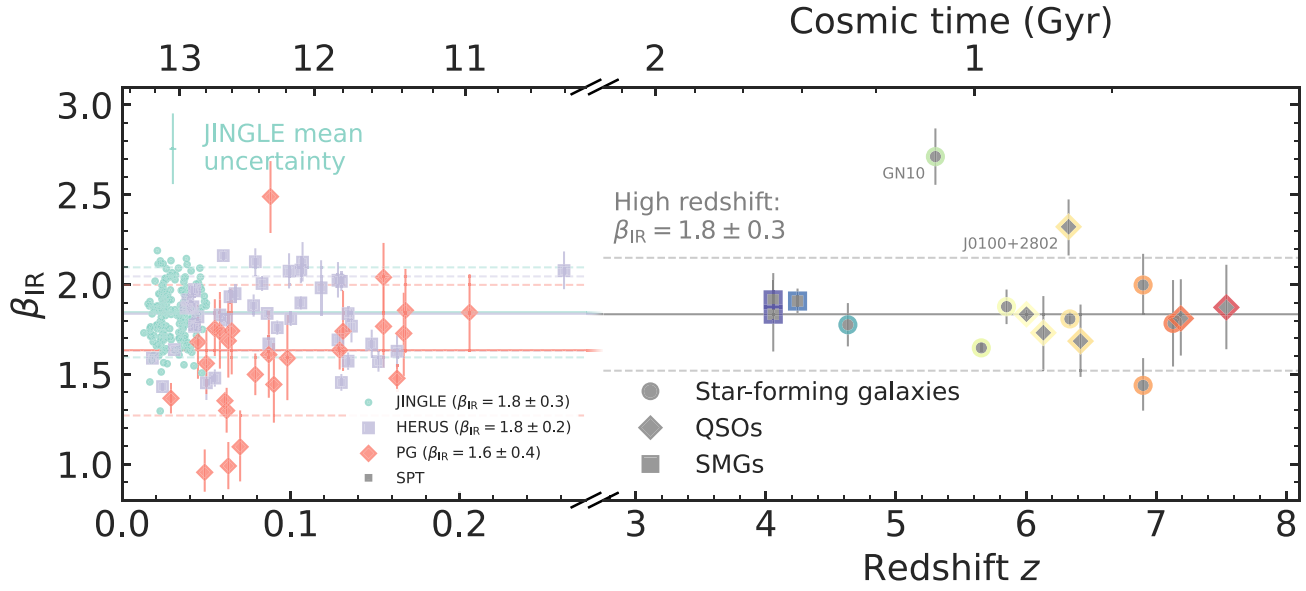

Figure 1. Cosmic evolution of the dust emissivity index β_{IR}. The sample of high-redshift galaxies (coloured according to redshift) is described in Section 2.2. At late times, results are shown for JINGLE galaxies (whose mean uncertainty is indicated instead of individual error bars for visualization purposes), (U)LIRGs from the HERUS survey, and QSOs from the PG sample (Section 2.1). Solid (dashed) horizontal lines indicate each sample's mean dust emissivity index (and scatter), consistent across JINGLE, HERUS, and high-redshift samples ($\beta_{IR} \simeq 1.8$) while slightly lower for the PG sample ($\beta_{IR} \simeq 1.6$).

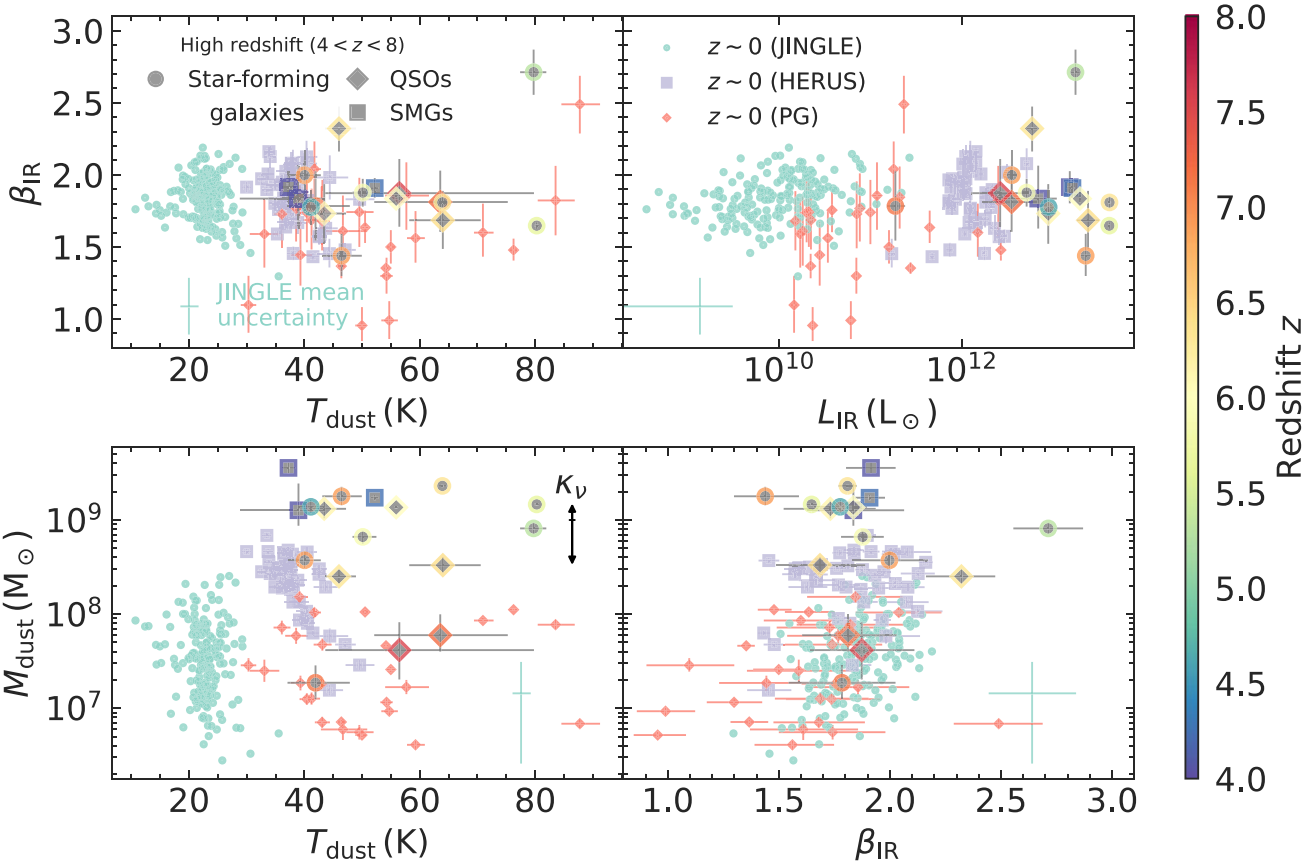

Figure 2. Interdependence of several dust properties: the dust emissivity index β_{IR}, temperature (T_{dust}), mass (M_{dust}), and the total IR luminosity (L_{IR}). Data points from the high-redshift sample are coloured according to their redshift. In each panel, instead of individual error bars the mean uncertainty of JINGLE galaxies is indicated for visualization purposes. In the lower left-hand panel, an arrow shows the systematic uncertainty on dust masses given the range of possible dust absorption cross-sections (κ_ν; see Witstok et al. 2022).

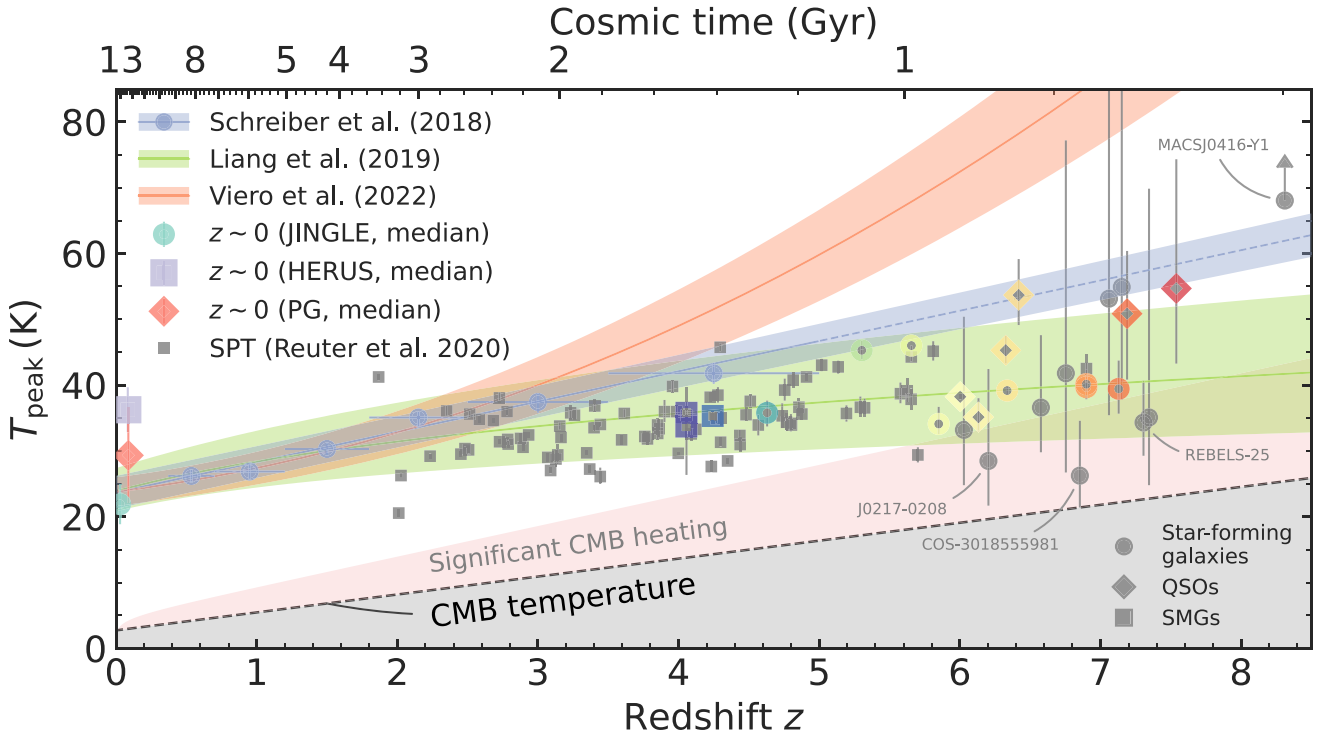

Figure 3. Dust peak temperature, $T_{\rm peak}$, as a function of cosmic time. Data points from the high-redshift sample are coloured according to their redshift (symbols are the same as before). Observed trends inferred by Schreiber et al. (2018) and Viero et al. (2022) from stacked spectra are shown, as is the power-law fit to the peak-temperature evolution of simulated galaxies by Liang et al. (2019). Sources from the SPT sample (Reuter et al. 2020) that have been refitted for consistency (see text for details) are shown as grey squares. We furthermore include several galaxies for which only two to three photometric data points are available to highlight the increased uncertainty (grey points without coloured edge, sources with an extreme dust temperature are annotated; see Section 3.2 for details). The grey dashed line indicates the CMB temperature, while the light-red area above shows the region where CMB heating is significant (more than 1 per cent difference compared to $z = 0$; see Witstok et al. 2022, for details).

To explore evolutionary trends in the dust temperature, Fig. 3 shows the observed peak temperature as a function of redshift for our sample of sources with well-sampled SEDs, whose temperature can therefore be accurately determined. To aid comparison between samples, we show empirical peak temperatures instead of the more opacity-dependent SED temperature $T_{\rm dust}$ (e.g. Casey et al. 2014; Cortzen et al. 2020). We also include several galaxies to highlight the increased uncertainty when only two to three photometric data points are available (all temperatures are inferred consistently with the fitting procedure described in Section 2.3). These are MACSJ0416-Y1 (Tamura et al. 2019; Bakx et al. 2020), B14−65666 (Bowler et al. 2018; Hashimoto et al. 2019; Sugahara et al. 2021), J1211−0118, J0217−0208 (Harikane et al. 2020), COS-3018555981, UVISTA-Z-001, UVISTA-Z-019 (Witstok et al. 2022), REBELS-12, REBELS-25, and REBELS-38 (Inami et al. 2022; Algera et al. 2023). Observed trends inferred by Schreiber et al. (2018) and Viero et al. (2022) from stacked spectra are shown (we note that the latter represents the SED temperature $T_{\rm dust}$ inferred using an optically thin SED), as is the power-law fit to the peak-temperature evolution of simulated galaxies (Liang et al. 2019). In addition, we include sources from the SPT survey (Section 2.2) in this comparison, since the emergent peak temperature can be determined directly from the observed SED and does not strongly depend on the underlying dust opacity (see e.g. Casey et al. 2014).[4] For consistency, however, we refitted these SEDs with an optically thin SED model, noting that there is little difference in the inferred peak temperatures.

Generally, the sources appear to follow the mild temperature evolution found by Liang et al. (2019) reasonably well. As is clear from Fig. 3, this is in agreement with trends reported in previous studies of the SPT sources (Reuter et al. 2020). Furthermore, a mildly rising temperature is in line with an evolving main sequence in combination with a non-evolving $L_{\rm IR}$–$T_{\rm peak}$ relation, as demonstrated at $0 < z < 2$ by Drew & Casey (2022). Moreover, from a theoretical perspective it is naturally expected that dust temperatures increase towards high redshift as a result of decreasing gas depletion times (Sommovigo et al. 2022a, b). A few sources, however, are clearly offset from this relation derived for SFGs. In particular, MACSJ0416-Y1 appears to contain exceptionally hot dust (see Bakx et al. 2020), while J0217−0208, COS-3018555981, and REBELS-25 have notably low temperatures (see also Witstok et al. 2022). (U)LIRGs from the HERUS sample have increased dust temperatures indicative of a more efficient (i.e. higher UV optical depth) and/or additional heating mechanism (e.g. Hirashita & Chiang 2022; Sommovigo et al. 2022a). The same is true for QSOs from the PG sample as well as several high-redshift quasars (in agreement with previous studies; e.g. McKinney et al. 2021; Walter et al. 2022).

[4]We note that the same does not hold for the SED dust temperature, $T_{\rm dust}$: two sources, GN10 and SPT0346−52, are fitted to have an intrinsically high dust temperature (Fig. 2), while the peak temperature is moderate, owing to their high optical depths.

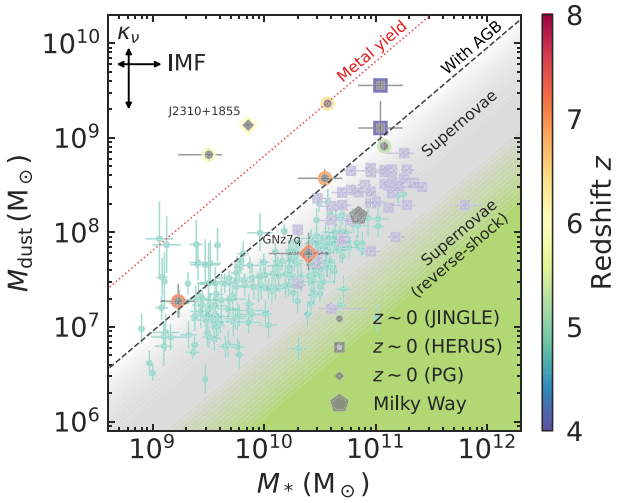

Figure 4. Galaxy dust masses as a function of stellar mass. Data points from the high-redshift sample are coloured according to their redshift (symbols are the same as before). Two QSOs whose stellar mass has been deduced from the dynamical and gas masses (Section 2.2) are annotated. Symbols are the same as in Figs 1 and 2, with the addition of the estimated stellar and dust masses of the Milky Way (Ginolfi et al. 2018). Grey shading indicates the region where SNe can be fully responsible for the dust production, green shading shows the same but with a significant reduction due to ∼95 per cent reverse-shock destruction. A maximum yield with additional contribution from AGB stars is indicated by the black dashed line. The edges are blurred on purpose to illustrate the systematic uncertainty in the choice of IMF when calculating the dust yield for a given stellar mass, with the red dotted line showing the highest metal yield, which translates into the maximum dust mass allowed (Section 3.3). As in Figs 1 and 2, an arrow shows the systematic uncertainty on dust masses given the range of possible dust absorption cross-sections (the current choice appropriate for dust ejected by SNe; see Section 3.3), while a second arrow shows the systematic change in observed stellar masses depending on the IMF (see text for details).

3.3 Dust masses at $4 < z < 8$

The derived dust masses are shown as a function of the stellar mass (if available; see Section 2.2) in Fig. 4. In our analysis, we focus on dust production by stellar sources: SN explosions, which are generally thought to be the main stellar source of dust in the early Universe, and AGB stars, which act on longer time-scales (e.g. Valiante et al. 2009; Mancini et al. 2015; Liu & Hirashita 2019; Burgarella et al. 2020; Nanni et al. 2020). As outlined in Section 2.3, there is a systematic uncertainty accompanying the choice of the dust absorption cross-section (visualized by an arrow, also shown in Figs 1 and 2; see Witstok et al. 2022). For consistency, the current choice is appropriate for dust ejected by SNe after reverse-shock destruction (Hirashita et al. 2014).

To relate the stellar and dust masses, we consider an IMF-averaged dust yield $\bar{y}_{\rm dust}$, which represents the mean dust mass formed per unit stellar mass and thus translates into a straight line in the dust versus stellar mass plane (i.e. a constant dust-to-stellar mass ratio, $M_{\rm dust}/M_*$). Given the uncertainty surrounding theoretical dust yields, in Fig. 4, we indicate a range of dust yields in a scenario where dust is produced by SNe and/or AGB stars under various IMFs following the method described in Di Cesare et al. (2023). Our aim here is to provide a simple prediction of the contribution of stellar sources to the observed dust masses, starting from a given set of theoretically motivated, mass-dependent yields (while varying the stellar IMF). We emphasize that this approach differs from the empirical method of Michałowski (2015) where, inversely, the yield per AGB star or SN event required to explain a given dust mass is inferred (see also Leśniewska & Michałowski 2019; Bakx et al. 2021; Schouws et al. 2022; Sommovigo et al. 2022b; Witstok et al. 2022).

The first scenario from Di Cesare et al. (2023) assumes a stellar age of 35 Myr where only the most massive stars ($M > 8\,{\rm M}_\odot$) contribute to the metal and dust budget through core-collapse SNe. This is shown both for the case where a significant fraction (∼95 per cent) of dust is destroyed by reverse-shock destruction and for the highly optimistic case of no destruction at all (cf. Ginolfi et al. 2018). The second has a stellar age of 650 Myr (approximately the Hubble time at $z \sim 7$) and includes additional enrichment by lower mass AGB stars ($M > 2.5\,{\rm M}_\odot$). These two scenarios are chosen to respectively highlight the contribution by SNe alone and the combination of SN and AGB stars. Where available (predominantly in the form of a gas depletion time), estimates of the stellar ages of the high-redshift sources considered in this work are consistently of the order of several tens of millions of years (e.g. Watson et al. 2015; Riechers et al. 2020), therefore suggesting that the dust production by AGB stars is minimal. We note that changing the stellar age only marginally changes the yield: in the first scenario, the most massive stars have smaller ejecta (resulting in a change of ∼10 per cent for an age range of 20–35 Myr), while the AGB contribution in any case is subdominant such that different ages in the second scenario do not significantly change the overall yield. We note that although the timing and grain composition of dust production by SN is uncertain, the adopted yields (0.16 and 0.66 M$_\odot$; Bianchi & Schneider 2007) are within the range of values reported in the literature and certainly are not expected to be significantly higher (e.g. Sarangi & Cherchneff 2015; Lazzati & Heger 2016; Marassi et al. 2019; Brooker et al. 2022).

The gradual diminishing of the shaded area corresponds to the range of yields obtained with various IMFs: a Salpeter (1955), Chabrier, top-heavy ($\alpha = 1.5$), and finally several Larson (1998) IMFs (with characteristic masses $M_{\rm ch}$ of 0.35, 5, and 10 M$_\odot$; see also Valiante et al. 2009). Yields range from $\bar{y}_{\rm SN} = 0.001\,59$ ($\bar{y}_{\rm SN+AGB} = 0.001\,83$) for a Salpeter IMF up to $\bar{y}_{\rm SN} = 0.008\,84$ ($\bar{y}_{\rm SN+AGB} = 0.008\,99$) for a Larson IMF ($M_{\rm ch} = 10\,{\rm M}_\odot$), which reduce to, respectively, $\bar{y}_{\rm SN} = 1.1 \times 10^{-4}$ ($\bar{y}_{\rm SN+AGB} = 3.46 \times 10^{-4}$) and $\bar{y}_{\rm SN} = 6.22 \times 10^{-4}$ ($\bar{y}_{\rm SN+AGB} = 9.14 \times 10^{-4}$, but in this case for $M_{\rm ch} = 5\,{\rm M}_\odot$) in the presence of a reverse shock causing ∼95 per cent destruction. These yields broadly match more detailed models, which also include the effects of dust reprocessing in the ISM (destruction by SN shocks, astration, ejection in outflows, and grain growth). Such analyses predict dust-to-stellar mass ratios depending on stellar mass and redshift, performed in semi-analytical setting (e.g. Mancini et al. 2015; Popping, Somerville & Galametz 2017; Vijayan et al. 2019; Dayal et al. 2022) and cosmological hydrodynamical simulations (e.g. McKinnon et al. 2017; Aoyama et al. 2018; Aoyama, Hirashita & Nagamine 2020; Graziani et al. 2020; Di Cesare et al. 2023): for instance, Di Cesare et al. (2023) predict $M_{\rm dust}/M_* \approx 3 \times 10^{-4}$ for $M_* \sim 10^9\,{\rm M}_\odot$ to $M_{\rm dust}/M_* \approx 10^{-2}$ for $M_* \sim 10^{11}\,{\rm M}_\odot$.

From Fig. 4, it appears that local galaxies (mostly) exhibit dust-to-stellar mass ratios consistent with the adopted dust yields, with a possible exception at low stellar masses ($M_* \lesssim 4 \times 10^9\,{\rm M}_\odot$) where a small fraction of SFGs from the JINGLE sample nominally exceed the maximum yield of SN and AGB stars combined. It appears that little room is left for a (significant) fraction of SN dust to be subsequently destroyed by the various processes mentioned above, or otherwise that any loss is made up by grain growth (see e.g. Valiante et al. 2011, 2014; Graziani et al. 2020; Dayal et al. 2022).

The high-redshift galaxies for which a measurement of the stellar mass is available paint a more drastic picture still: a significant fraction are located either in a region where ∼95 per cent reverse-shock destruction is strongly ruled out (i.e. approximately on the black dashed line; four out of nine sources), or indeed where even the optimistic SN and AGB dust yields combined appear inadequate in accounting for the observed dust mass (i.e. significantly above the black dashed line; an additional four out of nine sources). We note that the latter four sources (MORA-4 also known as MAMBO-9, J2310+1855, HFLS3, and GN20) are some of the FIR-brightest and highly starburst (in the case of J2310+1855, quasar-host) galaxies known, likely or demonstrably located within highly overdense regions of the early Universe (Riechers et al. 2013; Tan et al. 2014; Casey et al. 2019; Tripodi et al. 2022). In this case, other dust production mechanisms, such as direct grain growth in the ISM, may need to be evoked (see also e.g. Valiante et al. 2014; Schneider, Hunt & Valiante 2016; Popping et al. 2017; Graziani et al. 2020; Di Cesare et al. 2023). However, we note that direct grain growth may not adequately resolve the tension as this process has been shown to become inefficient in dense molecular clouds due to the formation of icy mantles (Ferrara et al. 2016; Ceccarelli et al. 2018). Moreover, two out of the offending data points are incompatible even with the maximum dust mass that is physically allowed – assuming that all metals are locked up in dust grains – even for the maximum metal yield out of all scenarios described above ($y_Z = 0.0641$ on a longer time-scale for a Larson IMF with $M_{\rm ch} = 10\,{\rm M}_\odot$). We note that although metal and dust yields at a fixed stellar mass are higher for top-heavy IMFs, the observed stellar masses currently inferred with a Chabrier IMF will also be reduced (as indicated by the arrow in Fig. 4), again worsening the discrepancy. This suggests that, independent of the IMF assumed, stellar mass estimates may be systematically low, in particular for the high-redshift sources (in agreement with recent findings suggesting that the stellar masses can vary up to ∼1 dex under a different star formation history; see Topping et al. 2022). Improved stellar mass estimates with *JWST* will significantly reduce their uncertainty, though we note that high dust yields are not only seen for galaxies whose stellar mass has been measured with SED fitting, but also via the dynamical mass (i.e. for J2310+1855; however, dynamical mass estimates equally carry significant uncertainty as they require many assumptions to be made in the dynamical modelling and gas mass inference; cf. Feruglio et al. 2018; Tripodi et al. 2022).

The inconsistency may therefore also be alleviated with a lower dust absorption cross-section, which directly increases the inferred dust masses. Due to spatial offsets between the light from (un-obscured) stars, ionized gas, and dust (e.g. Carniani et al. 2017; Behrens et al. 2018; Bowler et al. 2018, 2022; Cochrane et al. 2019; Inami et al. 2022), integrated measures such as the stellar mass and dust mass could in reality trace different components. A more heterogeneous dust distribution, for example in a scenario with multiple star-forming regions enshrouded by dust to varying degrees, might bias spatially resolved observations to trace optically thick dust efficiently heated by stars, while colder, possibly more extended dust reservoirs remain undetected (e.g. Ferrara et al. 2017; Akins et al. 2022; Witstok et al. 2022). High-resolution, multiwavelength follow-up observations (with e.g. ALMA and *JWST*) are required to confirm this.

4 SUMMARY AND CONCLUSIONS

We applied a flexible fitting routine to the dust-continuum emission of a sample of 17 galaxies in the early Universe ($4 < z < 8$) with well-sampled FIR SEDs, consisting of 6 quasars (QSOs), 8 SFGs, and 3 SMGs. We put the results into context by comparing to two samples of nearby galaxies. We constrain the dust mass, temperature, emissivity index, and opacity of each source within a Bayesian inference framework to characterize collective trends of the dust properties. We summarize our findings as follows:

(i) We find no significant evolution in the dust emissivity index across cosmic time, measuring a consistent value of $\beta_{\rm IR} \simeq 1.8$ for the local samples of SFGs and (U)LIRGs as well as in the high-redshift sample, while it is slightly lower for the sample of local QSOs ($\beta_{\rm IR} \simeq 1.6$). This suggests that the effective properties of dust do not change dramatically, though we note that our selection criteria might introduce a bias towards the IR-brightest sources. GN10 and J0100+2802, with $\beta_{\rm IR} \simeq 2.7$ and 2.3, respectively, are two notable exceptions among the galaxies considered here.

(ii) In other dust properties, we find the high-redshift galaxies to be similar to, or in dust temperature and IR luminosity even more extreme than, (U)LIRGs in the HERUS sample. The dust temperature in our high-redshift sample points towards a mild evolution with redshift, though several of the most distant quasars, like local quasars and (U)LIRGs, exhibit elevated temperatures pointing towards an additional and/or more efficient heating mechanism.

(iii) For a subsample of galaxies, we compare stellar mass estimates with our inferred dust masses, whose degeneracy mainly with dust temperature is reduced for well-constrained SEDs. About half of the cases fall within a simple, IMF-averaged dust yield of stellar sources alone (i.e. SNe and AGB stars), provided no destruction in the ISM or ejection from the galaxy takes place. The other half, however, exceeds a highly optimistic yield by up to an order of magnitude, suggesting that stellar masses are underestimated or metal yields are seemingly violated, both implying that the mass-to-light ratio of dust may be systematically overestimated.

ACKNOWLEDGEMENTS

We are grateful to Stephen Eales and Laura Sommovigo for fruitful discussions. We further thank the anonymous referee for the helpful suggestions. JW, GCJ, RM, and RSm acknowledge support from the European Research Council (ERC) Advanced Grant 695671, 'QUENCH'. JW furthermore gratefully acknowledges support from the Fondation MERAC. GCJ acknowledges funding from ERC Advanced Grant 789056 'FirstGalaxies'. RM also acknowledges funding from a research professorship from the Royal Society. RSm acknowledges a Science and Technology Facilities Council (STFC) Ernest Rutherford Fellowship (ST/S004831/1). RSc acknowledges support from the Amaldi Research Center funded by the MIUR programme 'Dipartimento di Eccellenza' (CUP:B81I18001170001). This work has also used the following packages in PYTHON: the SCIPY library (Jones et al. 2001), its packages NUMPY (van der Walt, Colbert & Varoquaux 2011) and MATPLOTLIB (Hunter 2007), the ASTROPY package (Astropy Collaboration 2013, 2018), and the PYMULTINEST package (Feroz, Hobson & Bridges 2009; Buchner et al. 2014).

DATA AVAILABILITY

No new data were generated or analysed in support of this research.

REFERENCES

Akins H. B. et al., 2022, ApJ, 934, 64
Algera H. et al., 2023, preprint (arXiv:2301.09659)

Aoyama S., Hou K.-C., Hirashita H., Nagamine K., Shimizu I., 2018, MNRAS, 478, 4905
Aoyama S., Hirashita H., Nagamine K., 2020, MNRAS, 491, 3844
Aravena M. et al., 2016, MNRAS, 457, 4406
Astropy Collaboration, 2013, A&A, 558, A33
Astropy Collaboration, 2018, AJ, 156, 123
Bakx T. J. L. C. et al., 2020, MNRAS, 493, 4294
Bakx T. J. L. C. et al., 2021, MNRAS, 508, L58
Beelen A., Cox P., Benford D. J., Dowell C. D., Kovács A., Bertoldi F., Omont A., Carilli C. L., 2006, ApJ, 642, 694
Behrens C., Pallottini A., Ferrara A., Gallerani S., Vallini L., 2018, MNRAS, 477, 552
Bertoldi F., Carilli C. L., Cox P., Fan X., Strauss M. A., Beelen A., Omont A., Zylka R., 2003, A&A, 406, L55
Bianchi S., Schneider R., 2007, MNRAS, 378, 973
Bouwens R. et al., 2020, ApJ, 902, 112
Bowler R. A. A., Bourne N., Dunlop J. S., McLure R. J., McLeod D. J., 2018, MNRAS, 481, 1631
Bowler R. A. A., Cullen F., McLure R. J., Dunlop J. S., Avison A., 2022, MNRAS, 510, 5088
Brooker E. S., Stangl S. M., Mauney C. M., Fryer C. L., 2022, ApJ, 931, 85
Buchner J. et al., 2014, A&A, 564, A125
Burgarella D., Nanni A., Hirashita H., Theulé P., Inoue A. K., Takeuchi T. T., 2020, A&A, 637, A32
Calzetti D., Armus L., Bohlin R. C., Kinney A. L., Koornneef J., Storchi-Bergmann T., 2000, ApJ, 533, 682
Carniani S. et al., 2017, A&A, 605, A42
Carniani S. et al., 2019, MNRAS, 489, 3939
Casey C. M. et al., 2013, MNRAS, 436, 1919
Casey C. M., Narayanan D., Cooray A., 2014, Phys. Rep., 541, 45
Casey C. M. et al., 2019, ApJ, 887, 55
Casey C. M. et al., 2021, ApJ, 923, 215
Ceccarelli C., Viti S., Balucani N., Taquet V., 2018, MNRAS, 476, 1371
Chabrier G., 2003, PASP, 115, 763
Chen L.-H., Hirashita H., Hou K.-C., Aoyama S., Shimizu I., Nagamine K., 2018, MNRAS, 474, 1545
Cheng C. et al., 2020, ApJ, 898, 33
Cicone C. et al., 2015, A&A, 574, A14
Clements D. L. et al., 2018, MNRAS, 475, 2097
Cochrane R. K. et al., 2019, MNRAS, 488, 1779
Cortzen I. et al., 2020, A&A, 634, L14
Cox P. et al., 2011, ApJ, 740, 63
Dayal P. et al., 2022, MNRAS, 512, 989
Di Cesare C., Graziani L., Schneider R., Ginolfi M., Venditti A., Santini P., Hunt L. K., 2023, MNRAS, 519, 4632
Draine B. T., 1989, in Böhm-Vitense E., ed., ESA SP-290: Infrared Spectroscopy in Astronomy. ESA, Noordwijk, p. 93
Draine B. T., 2003, ARA&A, 41, 241
Draine B. T., 2009, in Henning T., Grün E., Steinacker J., eds, ASP Conf. Ser. Vol. 414, Cosmic Dust – Near and Far. Astron. Soc. Pac., San Francisco, p. 453
Draine B. T. et al., 2007, ApJ, 663, 866
Drew P. M., Casey C. M., 2022, ApJ, 930, 142
Dwek E., 1998, ApJ, 501, 643
Faisst A. L., Fudamoto Y., Oesch P. A., Scoville N., Riechers D. A., Pavesi R., Capak P., 2020, MNRAS, 498, 4192
Feroz F., Hobson M. P., Bridges M., 2009, MNRAS, 398, 1601
Ferrara A., Viti S., Ceccarelli C., 2016, MNRAS, 463, L112
Ferrara A., Hirashita H., Ouchi M., Fujimoto S., 2017, MNRAS, 471, 5018
Ferrara A. et al., 2022, MNRAS, 512, 58
Feruglio C. et al., 2018, A&A, 619, A39
Fudamoto Y. et al., 2020, A&A, 643, A4
Fudamoto Y. et al., 2021, Nature, 597, 489
Fujimoto S. et al., 2022, Nature, 604, 261
Gallerani S., Ferrara A., Neri R., Maiolino R., 2014, MNRAS, 445, 2848
Ginolfi M., Graziani L., Schneider R., Marassi S., Valiante R., Dell'Agli F., Ventura P., Hunt L. K., 2018, MNRAS, 473, 4538
Graziani L., Schneider R., Ginolfi M., Hunt L. K., Maio U., Glatzle M., Ciardi B., 2020, MNRAS, 494, 1071
Harikane Y. et al., 2020, ApJ, 896, 93
Hashimoto T. et al., 2019, PASJ, 71, 71
Hirashita H., Chiang I.-D., 2022, MNRAS, 516, 1612
Hirashita H., Ferrara A., Dayal P., Ouchi M., 2014, MNRAS, 443, 1704
Hunter J. D., 2007, Comput. Sci. Eng., 9, 90
Inami H. et al., 2022, MNRAS, 515, 3126
Inoue A. K., Hashimoto T., Chihara H., Koike C., 2020, MNRAS, 495, 1577
Jarugula S. et al., 2021, ApJ, 921, 97
Jiménez-Andrade E. F. et al., 2020, ApJ, 890, 171
Jin S. et al., 2022, A&A, 665, A3
Jones E., Oliphant T., Peterson P., 2001, SciPy: Open Source Scientific Tools for Python. Available at: http://www.scipy.org/
Jones A. P., Fanciullo L., Köhler M., Verstraete L., Guillet V., Bocchio M., Ysard N., 2013, A&A, 558, A62
Jones G. C., Maiolino R., Caselli P., Carniani S., 2020, MNRAS, 498, 4109
Kelly B. C., Shetty R., Stutz A. M., Kauffmann J., Goodman A. A., Launhardt R., 2012, ApJ, 752, 55
Knudsen K. K., Watson D., Frayer D., Christensen L., Gallazzi A., Michałowski M. J., Richard J., Zavala J., 2017, MNRAS, 466, 138
Lamperti I. et al., 2019, MNRAS, 489, 4389
Laporte N., Nakajima K., Ellis R. S., Zitrin A., Stark D. P., Mainali R., Roberts-Borsani G. W., 2017, ApJ, 851, 40
Larson R. B., 1998, MNRAS, 301, 569
Lazzati D., Heger A., 2016, ApJ, 817, 134
Leśniewska A., Michałowski M. J., 2019, A&A, 624, L13
Li J. et al., 2020, ApJ, 889, 162
Liang L. et al., 2019, MNRAS, 489, 1397
Liu H.-M., Hirashita H., 2019, MNRAS, 490, 540
Madau P., Dickinson M., 2014, ARA&A, 52, 415
Magdis G. E. et al., 2011, ApJ, 740, L15
Magnelli B. et al., 2019, ApJ, 877, 45
Mancini M., Schneider R., Graziani L., Valiante R., Dayal P., Maio U., Ciardi B., Hunt L. K., 2015, MNRAS, 451, L70
Marassi S., Schneider R., Limongi M., Chieffi A., Graziani L., Bianchi S., 2019, MNRAS, 484, 2587
Marrone D. P. et al., 2018, Nature, 553, 51
McKinney J., Hayward C. C., Rosenthal L. J., Martínez-Galarza J. R., Pope A., Sajina A., Smith H. A., 2021, ApJ, 921, 55
McKinnon R., Torrey P., Vogelsberger M., Hayward C. C., Marinacci F., 2017, MNRAS, 468, 1505
Meurer G. R., Heckman T. M., Calzetti D., 1999, ApJ, 521, 64
Michałowski M. J., 2015, A&A, 577, A80
Nanni A., Burgarella D., Theulé P., Côté B., Hirashita H., 2020, A&A, 641, A168
Novak M. et al., 2019, ApJ, 881, 63
Omukai K., Tsuribe T., Schneider R., Ferrara A., 2005, ApJ, 626, 627
Pallottini A. et al., 2022, MNRAS, 513, 5621
Petric A. O., Ho L. C., Flagey N. J. M., Scoville N. Z., 2015, ApJS, 219, 22
Pope A. et al., 2006, MNRAS, 370, 1185
Popping G., Somerville R. S., Galametz M., 2017, MNRAS, 471, 3152
Reuter C. et al., 2020, ApJ, 902, 78
Riechers D. A. et al., 2009, ApJ, 703, 1338
Riechers D. A. et al., 2013, Nature, 496, 329
Riechers D. A. et al., 2020, ApJ, 895, 81
Robson I., Priddey R. S., Isaak K. G., McMahon R. G., 2004, MNRAS, 351, L29
Saintonge A. et al., 2018, MNRAS, 481, 3497
Salpeter E. E., 1955, ApJ, 121, 161
Sanders D. B., Mazzarella J. M., Kim D. C., Surace J. A., Soifer B. T., 2003, AJ, 126, 1607
Sarangi A., Cherchneff I., 2015, A&A, 575, A95
Savage B. D., Mathis J. S., 1979, ARA&A, 17, 73
Schaerer D. et al., 2020, A&A, 643, A3
Schneider R., Omukai K., Inoue A. K., Ferrara A., 2006, MNRAS, 369, 1437
Schneider R., Hunt L., Valiante R., 2016, MNRAS, 457, 1842
Schouws S. et al., 2022, ApJ, 928, 31

Schreiber C., Elbaz D., Pannella M., Ciesla L., Wang T., Franco M., 2018, A&A, 609, A30
Shao Y. et al., 2017, ApJ, 845, 138
Shao Y. et al., 2019, ApJ, 876, 99
Shen X., Vogelsberger M., Nelson D., Tacchella S., Hernquist L., Springel V., Marinacci F., Torrey P., 2022, MNRAS, 510, 5560
Smith M. W. L. et al., 2019, MNRAS, 486, 4166
Sommovigo L., Ferrara A., Pallottini A., Carniani S., Gallerani S., Decataldo D., 2020, MNRAS, 497, 956
Sommovigo L., Ferrara A., Carniani S., Zanella A., Pallottini A., Gallerani S., Vallini L., 2021, MNRAS, 503, 4878
Sommovigo L. et al., 2022a, MNRAS, 513, 3122
Sommovigo L. et al., 2022b, MNRAS, 517, 5930
Sugahara Y. et al., 2021, ApJ, 923, 5
Tamura Y. et al., 2019, ApJ, 874, 27
Tan Q. et al., 2014, A&A, 569, A98
Todini P., Ferrara A., 2001, MNRAS, 325, 726
Topping M. W. et al., 2022, MNRAS, 516, 975
Tripodi R. et al., 2022, A&A, 665, A107
Tripodi R. et al., 2023, ApJ, 946, L45
Valiante R., Schneider R., Bianchi S., Andersen A. C., 2009, MNRAS, 397, 1661
Valiante R., Schneider R., Salvadori S., Bianchi S., 2011, MNRAS, 416, 1916
Valiante R., Schneider R., Salvadori S., Gallerani S., 2014, MNRAS, 444, 2442
van der Walt S., Colbert S. C., Varoquaux G., 2011, Comput. Sci. Eng., 13, 22
Venemans B. P. et al., 2020, ApJ, 904, 130
Viero M. P., Sun G., Chung D. T., Moncelsi L., Condon S. S., 2022, MNRAS, 516, L30
Vijayan A. P., Clay S. J., Thomas P. A., Yates R. M., Wilkins S. M., Henriques B. M., 2019, MNRAS, 489, 4072
Vijayan A. P. et al., 2022, MNRAS, 511, 4999
Wakelam V. et al., 2017, Mol. Astrophys., 9, 1
Walter F. et al., 2022, ApJ, 927, 21
Wang F., Wang R., Fan X., Wu X.-B., Yang J., Neri R., Yue M., 2019, ApJ, 880, 2
Watson D., 2011, A&A, 533, A16
Watson D., Christensen L., Knudsen K. K., Richard J., Gallazzi A., Michałowski M. J., 2015, Nature, 519, 327
Weingartner J. C., Draine B. T., 2001, ApJ, 548, 296
Witstok J. et al., 2022, MNRAS, 515, 1751
Witstok J. et al., 2023, preprint (arXiv:2302.05468)
Younger J. D. et al., 2007, ApJ, 671, 1531
Zhukovska S., Dobbs C., Jenkins E. B., Klessen R. S., 2016, ApJ, 831, 147

SUPPORTING INFORMATION

Supplementary data are available at *MNRAS* online.

Corner_plots.zip.

Please note: Oxford University Press is not responsible for the content or functionality of any supporting materials supplied by the authors. Any queries (other than missing material) should be directed to the corresponding author for the article.

APPENDIX: FIR SED FITS

As an example, the posterior distributions for fitting the FIR SED of A1689-zD1 obtained with MERCURIUS under a self-consistent general opacity model are shown in Fig. A1. Similar figures for other sources in our sample (Table 2) are included in the Supplementary material.

In Fig. A2, we show the 'best-fitting' SED curve for the maximum likelihood in the ($M_{\rm dust}$, $T_{\rm dust}$) plane, while shaded regions indicate the uncertainty as the deviation of the 16th and 84th percentiles from the median (50th percentile) at each wavelength of all curves produced according to the posterior distribution. We show two types of fits: either in an entirely optically thin scenario (dashed lines) or with a self-consistent general opacity model, where we link the dust mass surface density, derived using the measured deconvolved area corresponding to the dust emission ($A_{\rm dust}$; see Table 2), to the optical depth (see Witstok et al. 2022, for details).

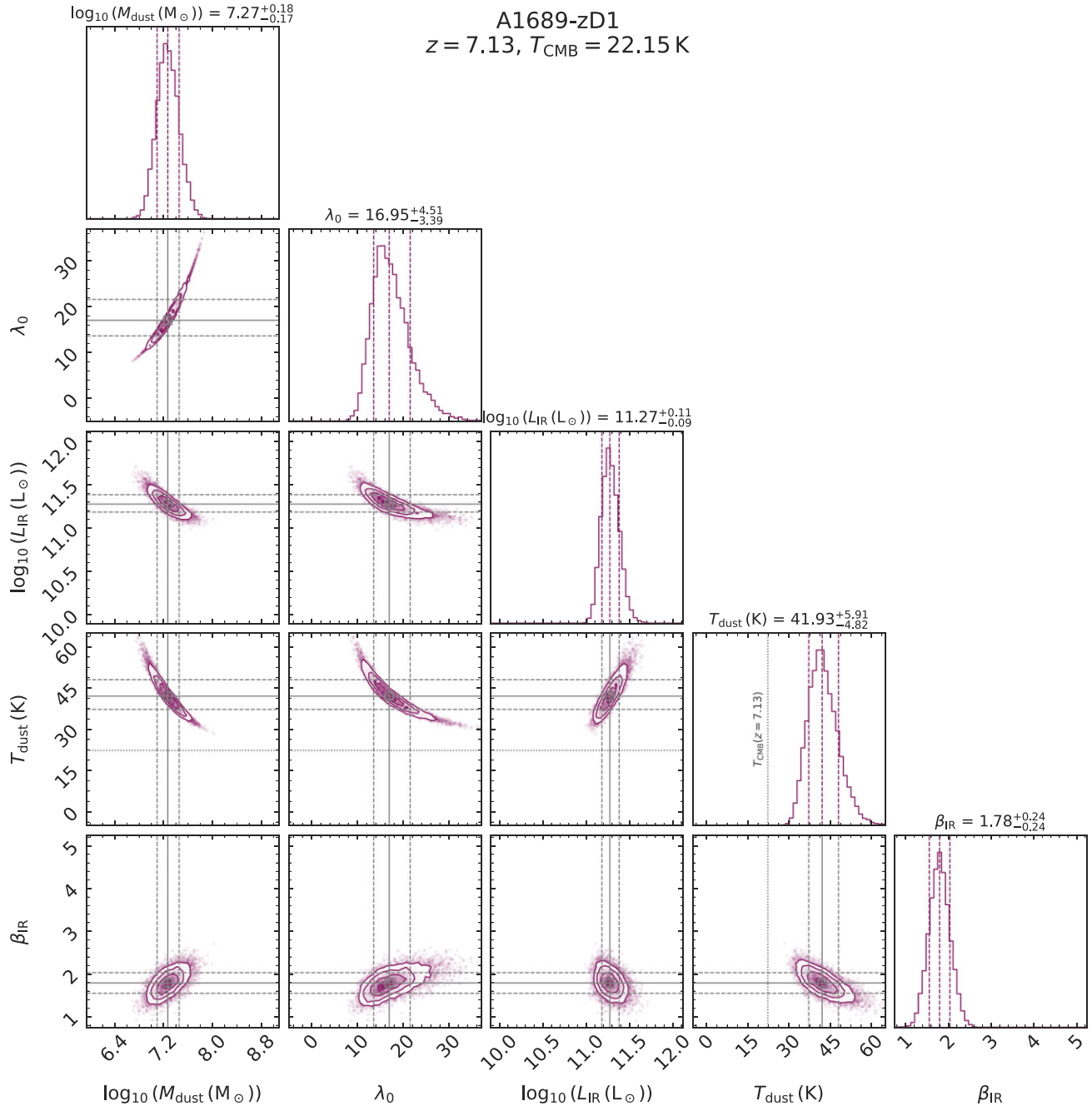

Figure A1. Posterior distributions for A1689-zD1 at $z = 7.13$ obtained in the FIR SED-fitting routine with MERCURIUS under a self-consistent general opacity model. Parameters shown are the dust mass ($M_{\rm dust}$), opacity transition wavelength (λ_0), total IR luminosity ($L_{\rm IR}$; note that this is included purely for visualization, not being an independent parameter in the fitting routine), dust temperature ($T_{\rm dust}$), and dust emissivity index ($\beta_{\rm IR}$). Solid grey lines indicate the median (i.e. 50th percentile) of the parameter's marginalized posterior distribution, while dashed lines show the 16th and 84th percentiles. In panels with the dust temperature, a dotted line indicates $T_{\rm CMB}$ ($z = 7.13$), the CMB temperature at the redshift of A1689-zD1.

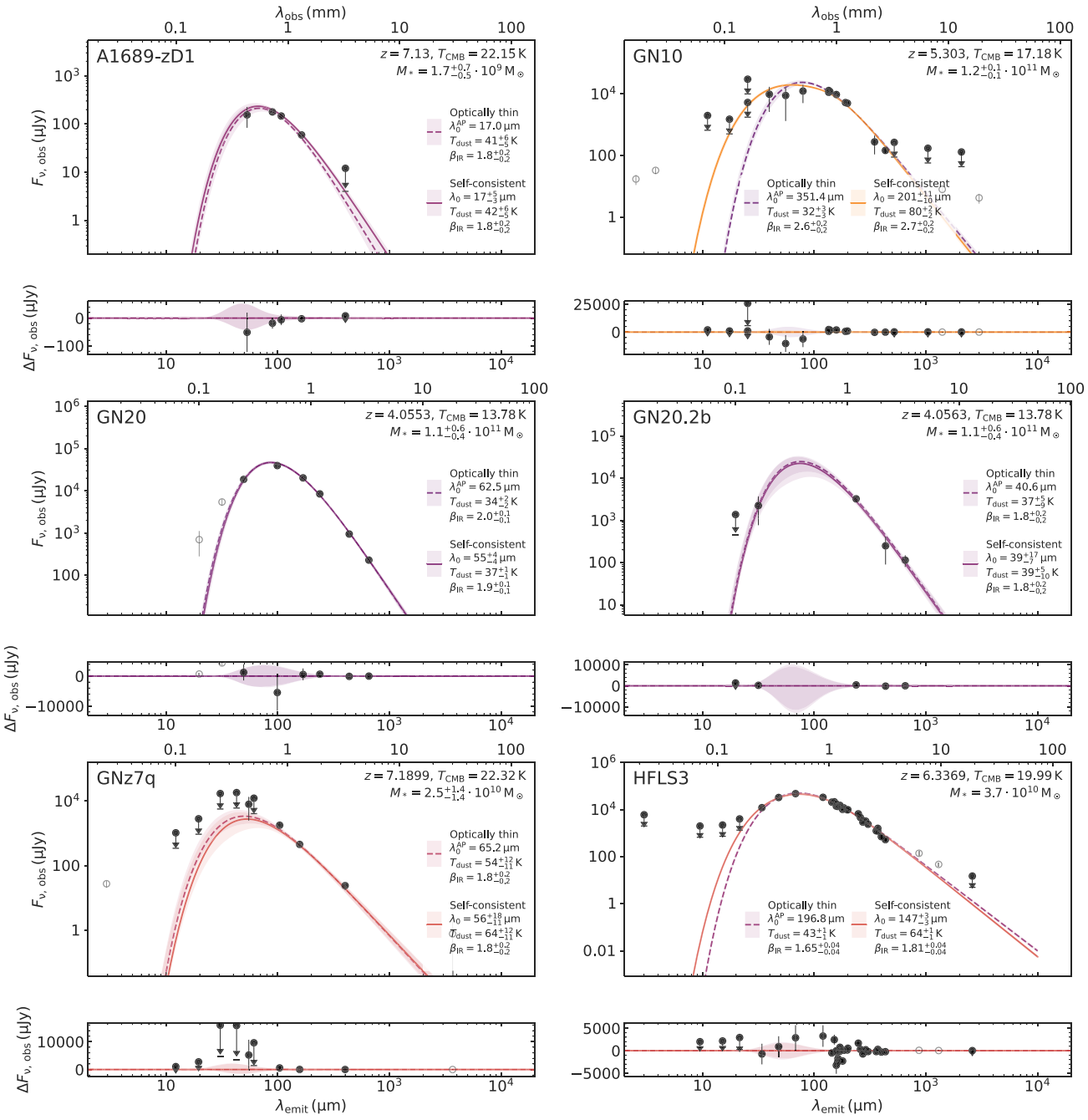

Figure A2. MERCURIUS fits to the FIR SEDs of the high-redshift sources considered in this work (Table 2). Photometric measurements and upper limits (3σ, with a vertical dash showing the 1σ level) are shown in black (open grey points are excluded from the fitting procedure; Section 2.3). Two types of fits are shown, either in an entirely optically thin scenario (dashed lines) or with a self-consistent optical depth model (solid lines; cf. Witstok et al. 2022). All dust properties derived using the latter model are listed in Table 3. Shaded regions indicate the uncertainty (see text for details). The label lists the transition wavelength (λ_0), dust temperature ($T_{\rm dust}$), and dust emissivity index ($\beta_{\rm IR}$). In the optically thin case, the transition wavelength is inferred AP ($\lambda_0^{\rm AP}$). A second, smaller panel below each fit shows the residuals ($\Delta F_{\nu,\,\rm obs}$) on a linear scale.

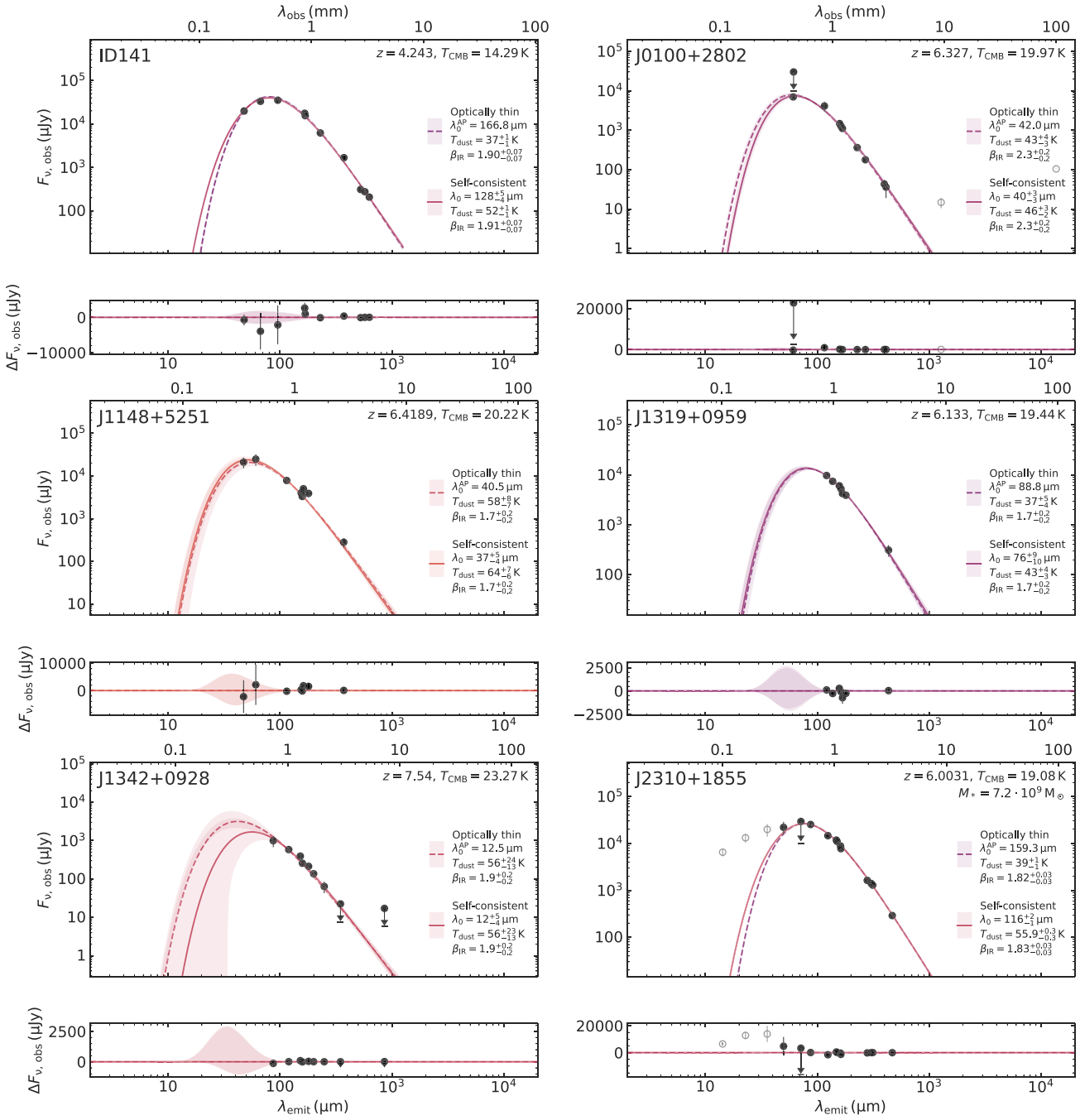

Figure A2. *Continued.*

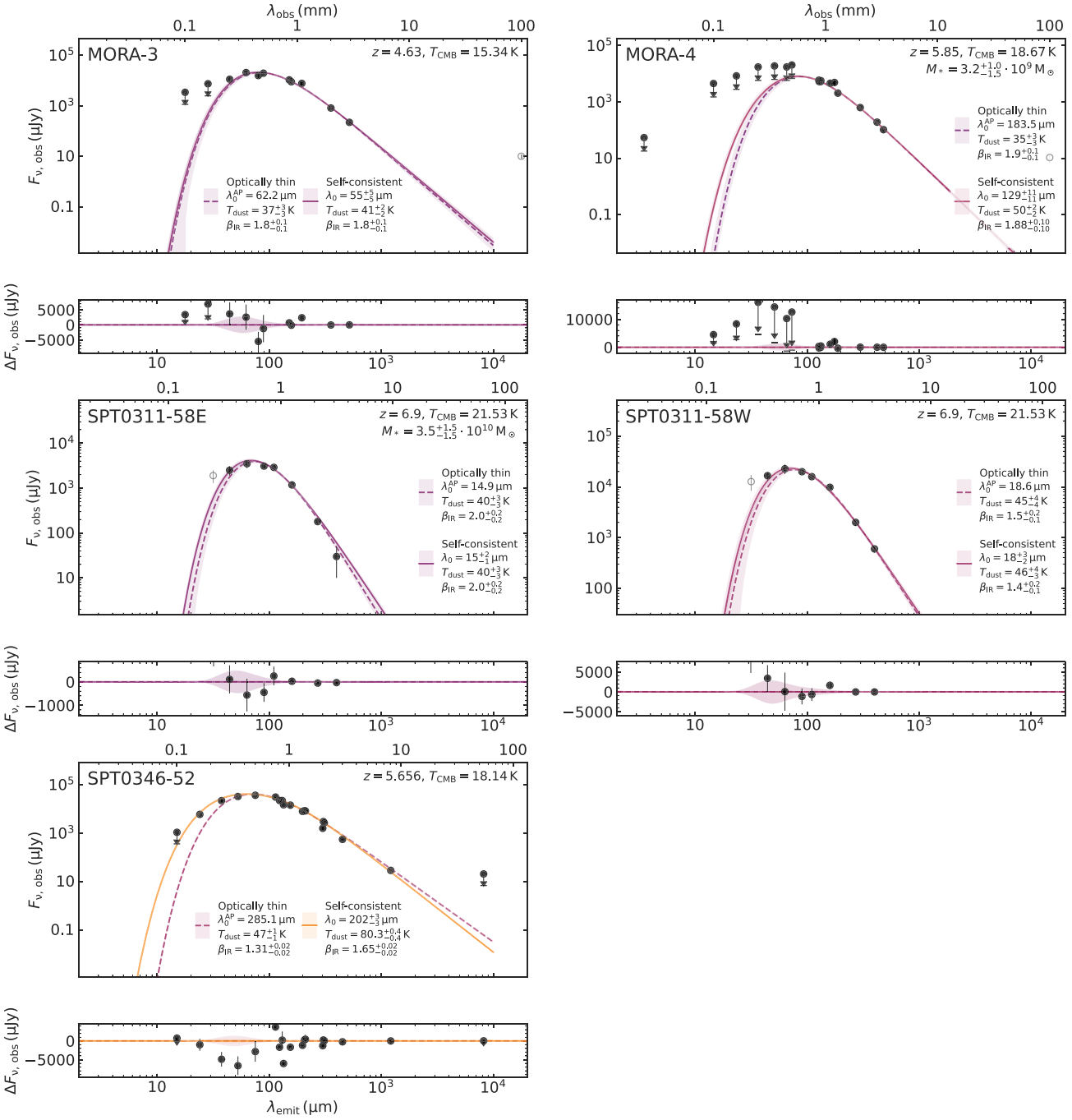

Figure A2. *Continued.*

This paper has been typeset from a TEX/LATEX file prepared by the author.